

Redox-Active Ultrathin Template of Silk Fibroin: Effect of Secondary Structure on Gold Nanoparticle Reduction

Eugenia Kharlampieva,[†] Dmitry Zimmitsky,[†] Maneesh Gupta,[†] Kathryn N. Bergman,[†]
David L. Kaplan,[‡] Rajesh R. Naik,[§] and Vladimir V. Tsukruk^{*,†}

[†]School of Materials Science and Engineering, Georgia Institute of Technology, Atlanta, Georgia 30332,

[‡]Department of Biomedical Engineering, Tufts University, Medford, Massachusetts 02155, and

[§]Air Force Research Laboratory, Materials and Manufacturing Directorate Wright-Patterson AFB,
Dayton, Ohio 45433

Received January 10, 2009. Revised Manuscript Received April 24, 2009

We report on an application of silk as an ultrathin redox-active template for controllable, one-step synthesis of gold nanoparticles via control over silk secondary structure. We found that both silk I and silk II molecular layers can facilitate gold nanoparticle formation at ambient conditions, indicating that tyrosine groups are available for metal ion reduction in both forms of silk. We suggest that the presence of β -sheets in silk II facilitates tyrosine ordering thereby resulting in well-dispersed, uniform nanoparticles with diameters of less than 6 nm. In addition, the mineralization does not result in transformation of the silk I secondary structure to silk II. In fact, the silk I structure is stabilized from further transformation into silk II even upon drying. These results are critical for developing a better understanding of silk interfacial behavior and offer an opportunity to design a new class of nanocomposites that combine the beneficial features of silk with those of the nanoparticles.

Introduction

The development of organic–inorganic nanocomposite materials which utilize biomolecules for the immobilization of inorganic nanoparticles has been receiving growing attention in bioengineering and materials science.^{1–11} Among a great variety of biomolecules, silk fibroin has been recently recognized as an attractive template for the synthesis of nano- and micro-inorganic structures due to a unique combination of biocompatibility, biodegradability, and excellent mechanical properties such as high tensile strength, high elasticity, and

exceptional toughness.^{12–19} Different inorganic materials such as silica, titania, zirconia, magnetite, apatite, silver chloride, and metal nanoparticles have been deposited or grown onto or within silk matrices to enhance mechanical and optical properties.^{20–32}

Silk-based materials with incorporated metal nanoparticles are of special interest since the nanocomposites have

*Corresponding author. E-mail: vladimir@mse.gatech.edu.

- (1) Angelatos, A. S.; Katagiri, K.; Caruso, F. *Soft Matter* **2006**, *2*, 18.
- (2) Chunmei, L.; Kaplan, D. *Curr. Opin. Solid. State. Mater. Sci.* **2003**, *7*, 265.
- (3) Mann, S. *Biomaterialization Principles and Concepts in Bioinorganic Materials Chemistry*; Oxford University Press: New York, 2001.
- (4) Harris, N.; Kohn, J. *Biomaterials Informatics*; John Wiley and Sons: New York, 2007.
- (5) Aizenberg, J. *Adv. Mater.* **2004**, *16*, 1295.
- (6) Stupp, S. I.; Donners, J.; Li, L.-S.; Mata, A. *MRS Bull.* **2005**, *30*, 864.
- (7) Davis, S.; Dujardin, E.; Mann, S. *Curr. Opin. Solid State Mater. Sci.* **2003**, *7*, 273.
- (8) Ludwigs, S.; Steiner, U.; Kulak, A. N.; Lam, R.; Meldrum, F. C. *Adv. Mater.* **2006**, *18*, 2270.
- (9) Gorna, K.; Munoz-Espi, R.; Groehn, F.; Wegner, G. *Macromol. Biosci.* **2007**, *7*, 163.
- (10) Brutchey, R. L.; Morse, D. E. *Chem. Rev.* **2008**, *108*, 4915.
- (11) Yusufoglu, Y.; Hu, Y.; Kanapathipillai, M.; Kramer, M.; Kalay, Y. E.; Thiagarajan, P.; Akinc, M.; Schmidt-Rohr, K.; Mallapragada, S. J. *Mater. Res.* **2008**, *23*, 3196.
- (12) Mang, Y.; Kim, H.-J.; Vunjak-Novakovic, G.; Kaplan, D. L. *Biomaterials* **2006**, *27*, 6064.
- (13) Guan, Z. *Polym. Int.* **2007**, *56*, 467.

- (14) Hakimi, O.; Knight, D. P.; Vollrath, F.; Vadgama, P. *Composites: Part B* **2007**, *38*, 324.
- (15) Shulha, H.; Foo, C. W. P.; Kaplan, D. L.; Tsukruk, V. V. *Polymer* **2006**, *47*, 5821.
- (16) Mayes, E. L.; Vollrath, F.; Mann, S. *Adv. Mater.* **1998**, *10*, 801.
- (17) Jiang, C.; Wang, X.; Gunawidjaja, R.; Lin, Y.-H.; Gupta, M. K.; Kaplan, D. L.; Naik, R. R.; Tsukruk, V. V. *Adv. Funct. Mater.* **2007**, *17*, 2229.
- (18) Lewis, R. *Chem. Rev.* **2006**, *106*, 3762.
- (19) Ebenstein, D. M.; Wahl, K. J. *J. Mater. Res.* **2006**, *21*, 2035.
- (20) Feng, X.-X.; Zhang, L.-L.; Chen, J.-Y.; Guo, Y.-H.; Zhang, H.-P.; Jia, C.-I. *Int. J. Biol. Macromol.* **2007**, *40*, 105.
- (21) Huang, L.; Wang, H.; Hayashi, C. Y.; Tian, B.; Zhao, D.; Yan, Y. *J. Mater. Chem.* **2003**, *13*, 666.
- (22) Li, C.; Jin, H.-J.; Botsaris, G. D.; Kaplan, D. L. *J. Mater. Res.* **2005**, *20*, 3374.
- (23) Dong, Q.; Su, H.; Zhang, D. *J. Phys. Chem. B* **2005**, *109*, 17429.
- (24) Singh, A.; Hede, S.; Sastry, M. *Small* **2007**, *3*, 466.
- (25) Cheng, C.; Shao, Z.; Vollrath, F. *Adv. Funct. Mater.* **2008**, *18*, 1.
- (26) Potiyaraj, P.; Kumlangdudsana, P.; Dubas, S. T. *Mater. Lett.* **2007**, *61*, 2464.
- (27) Feng, X.-X.; Chen, J.-Y.; Yao, J.-M.; Zhang, J.-C. *J. Appl. Polym. Sci.* **2006**, *101*, 2162.
- (28) He, J.; Kunitake, T. *Chem. Mater.* **2004**, *16*, 2656.
- (29) Furuzono, T.; Taguchi, T.; Kishida, A.; Akashi, M.; Tamada, Y. *J. Biomed. Mater. Res.* **2000**, *50*, 344.
- (30) Takeuchi, A.; Ohtsuki, C.; Miyazaki, T.; Tanaka, H.; Yamazaki, M.; Tanihara, M. *J. Biomed. Mater. Res.* **2003**, *65A*, 283.
- (31) Wong, P.; Patwardhan, S. V.; Belton, D. J.; Kitchel, B.; Anastasiades, D.; Huang, J.; Naik, R. R.; Perry, C. C.; Kaplan, D. L. *Proc. Natl. Acad. Sci. U.S.A.* **2006**, *103*, 9428.
- (32) Omenetto, F. G.; Kaplan, D. L. *Nat. Photonics* **2008**, *2*, 641.

been used for a range of biomedical and sensing applications, such as antibacterial coatings, thin film sensors, and plastic “memory” devices.^{33–35} Metal nanoparticles, specifically gold nanoparticles, possess remarkable biocompatibility and nontoxicity. Moreover, it is less oxidizable material than silver and thus can be utilized for long-term applications. Antibodies and proteins can be conjugated to gold nanoparticles through specific thiol-functionality, which makes them important for biochemical detection and therapeutic applications.^{36,37}

Silk templates were utilized as a matrix for incorporation of preformed silver nanoparticles³⁸ or for binding metal ions from solutions and their subsequent chemical reduction.^{39,40} Silk was also found to reduce metal ions from aqueous solution without the need for additional reducing agents, resulting in one-step in situ synthesis of metal nanoparticles at ambient conditions. This technique was applied to silk fibroin solutions at alkaline conditions to obtain colloidal core–shell gold–silk nanoparticles of high monodispersity.⁴¹ Silk microfibers with diameters of 2–5 μm have also been used as solid templates for reduction of silver²³ and gold²⁴ nano- and microparticles.

Despite major advancements in bioenabled synthesis of nanostructured materials, the synthesis of monodisperse, nonaggregated nanoparticles at the surface of solid substrates at ambient conditions remains a significant challenge. The prior work on silk-templated mineralization has mostly focused on micrometer-sized silk films or fibers. In addition, the size of inorganic particles on silk surfaces usually exceeded several micrometers with a broad particle size distribution and significant aggregation. Furthermore, the role of silk secondary structure on metal reduction as well as possible alternation of silk conformation as a result of metal reduction were not investigated.

It is worth noting that the transformation of silk secondary structure has been intensively studied in solutions and solid states.^{14,42,43,69–72} However, much less is known with regard to ultrathin silk films (< 10 nm) at water–solid or air–solid interfaces.^{54,17} For instance, solid silk films obtained by casting or electrospun fibers are composed of random coils and α -helices in the silk I state. Therefore, these materials are soluble in water and cannot be used for biomineralization at ambient

conditions. To convert silk I into the insoluble silk II state (β -sheets) and thus facilitate reduction experiments, treatment with methanol, annealing at high temperature, mechanical stretching, long-term storage, or UV irradiation are routinely utilized.⁴³

The lack of knowledge about secondary structure and properties of ultrathin silk films at interfaces can mostly be attributed to experimental difficulties in probing secondary structures for nanometer thick films. However, we believe that control over silk secondary structure at interfaces as well as the effect of silk conformations on gold reduction would be essential for obtaining a comprehensive picture about such a remarkable biomaterial.^{42,44}

Thus, in the present work we introduce a simple and versatile strategy to generate ultrathin (< 5 nm) nanocomposite silk films with homogeneously dispersed gold nanoparticles at ambient conditions. Control over nanoparticle size and distribution is achieved by controlling secondary structure of silk within a molecular-thin surface layer. Silk as a redox-active surface layer is found to preserve the native-like silk I structure in wet form, but can readily and immediately transform into silk II upon dehydration. We also demonstrated that both silk I and II forms are capable of metal reduction, and the reduction does not affect the initial secondary structures of silk surface layers for both silk I and II forms. In addition, silk I after being mineralized preserves its structure from further transformation into silk II upon drying.

Experimental Section

Materials. Poly(allylamine hydrochloride) (PAH, $M_w = 65\,000$), poly(sodium 4-styrenesulfonate) (PSS, $M_w = 70\,000$), cellulose acetate (50 000), borate buffer (pH 10), and HAuCl_4 solution were purchased from Aldrich. Nanopure water with a resistivity 18.2 $\text{M}\Omega\text{ cm}$ was used in all experiments. D_2O with 99.9% isotope content was purchased from Cambridge Isotope Laboratories and was used as received. To control pH and ionic strength, concentrated HCl and the inorganic salts NaCl, Na_2HPO_4 , and NaH_2PO_4 (General Storage, pure grade) were used as received.

Silk cocoons were obtained from *Bombyx mori* silkworms raised on a diet of Silkworm Chow (Mulberry Farms, Fallbrook, CA). Upon completion of the cocoons, the live pupae were extracted in order to avoid potential contamination or degradation of the fibroin protein. Sericin proteins were removed from the fibers following the procedure.⁴⁵ Silk cocoons were soaked at 3.3% (w/v) in a solution of 8 M urea containing 40 mM Tris- SO_4 and 0.5 M β -mercaptoethanol. The solution was heated to 90 $^\circ\text{C}$ for 1 h in a water bath. The silk fibers were stirred regularly to ensure complete removal of sericin proteins. The silk fibers were then removed and dried by centrifugation at 4000 rpm in a 50 mL tube. The fibers were then washed extensively with ultrapure distilled water (18 $\text{M}\Omega\text{-cm}$) and again dried by centrifugation. The washing procedure was repeated five times to ensure complete removal of trace urea and sericin from the fibers. The fibers were then lyophilized for 48–72 h to remove any residual water.

(33) Leong, W.; Lee, P.; Mhaisalkar, S.; Chen, T.; Dodabalapur, A. *Appl. Phys. Lett.* **2007**, *90*, 042906.

(34) Jiang, C.; Markutsya, S.; Pikus, Y.; Tsukruk, V. V. *Nat. Mater.* **2004**, *3*, 721.

(35) Gatesy, J.; Hayashi, C.; Motriuk, D.; Woods, J.; Lewis, R. *Science* **2001**, *291*, 2603.

(36) Riboh, J. C.; Haes, A. J.; McFarland, A. D.; Ranjit, C.; Van Duyne, R. P. *J. Phys. Chem. B* **2003**, *107*, 1772.

(37) El-Sayed, I. H.; Huang, X.; El-Sayed, M. A. *Cancer Lett.* **2006**, *239*, 129.

(38) Dubas, S.; Kumlangdudsana, P.; Potiyaraj, P. *Colloids Surfaces A* **2006**, *289*, 105.

(39) Ikawa, T.; Sajiki, H.; Hirota, K. *Tetrahedron* **2005**, *61*, 2217.

(40) Gulrajani, M. L.; Gupta, D.; Periyasamy, S.; Muthu, S. G. *J. Appl. Polym. Sci.* **2008**, *108*, 614.

(41) Zhou, Y.; Chen, W.; Itoh, H.; Naka, K.; Ni, Q.; Yamane, H.; Chujo, Y. *Chem. Commun.* **2001**, *23*, 2518.

(42) Tretinnikov, O. N.; Tamada, Y. *Langmuir* **2002**, *17*, 7406.

(43) Hardy, J. G.; Römer, L. M.; Scheibel, T. H. *Polymer* **2008**, *49*, 4309.

(44) Muller, W. S.; Samuelson, L. A.; Fossey, S. A.; Kaplan, D. L. *Langmuir* **1993**, *9*, 1867.

(45) Yamada, H.; Nakao, H.; Takasu, Y.; Tsubouchi, K. *Mater. Sci. Eng., C* **2001**, *14*, 41.

Dry silk fibers were subsequently dissolved in a 50 mL tube containing 9.3 M lithium bromide solution. The tube was placed in a hot water bath for 1 h to achieve complete dissolution according to published procedures.⁴⁵ The solution was centrifuged to remove impurities and degraded fraction. It was found that heating below 80 °C did not completely remove sericin from the fibers and short treatments for less than 1 h resulted in fibers that were difficult to dissolve. This may be a result of differences in the source of our silk cocoons. We acknowledge that there maybe some degradation of silk fibroin protein; however, all our experiments point to protein characteristics in accordance with the current literature. The solution was then dialyzed against distilled water using Slide-a-Lyzer dialysis cassettes (MWCO 3,500, Pierce) at room temperature for two days to remove the salt. Ultrapure distilled water was used to dilute the aqueous solution to the desired working condition of 0.2–0.5% for thin film fabrication.

Instrumentation. Silk deposition and gold formation were studied by a Dimension 3000 AFM microscope (Digital Instruments). AFM images were collected in the tapping mode with silicon tips with a spring constant of 50 N/m according to the procedure adapted in our group.^{46,47} The thicknesses of the silk layer and underlying (PAH/PSS) layers were measured with a spectroscopic ellipsometer M2000U (Woolam). Transmission electron microscopy (TEM) was performed with a JEOL 100CX-2 electron microscope at 100 kV. High-resolution TEM (HRTEM) images were obtained on a Hitachi HD-2000 Field Emission Gun (FEG) TEM at 200 kV. Energy dispersive X-ray (EDAX) spectra were collected on a Phillips CM200 TEM Lab6 operating at 200 kV equipped with a Thermo Electron EDAX detector. UV–vis spectra were recorded on a CARY spectrophotometer using quartz slides as templates.

Multilayer Deposition and Formation of Gold Nanoparticles. Multilayered films were obtained by alternating deposition of PAH and PSS by a spin-assisted LbL (SA-LbL) method as described in our previous publications.^{48–50} Specifically, 30 μ L of 1 mg/mL polyelectrolyte solutions were sequentially dropped on silicon substrates and rotated for 20 s with a 5000-rpm rotation speed rinsing twice with Nanopure water between the deposition cycles, starting from PAH. Thus, 2-bilayer (PAH/PSS)₂ or 2.5-bilayer (PAH/PSS)₂PAH films were constructed. Free-standing films were fabricated by initial deposition of a sacrificial layer of acetate cellulose from 2% solution in dioxane followed by 20-bilayer (PSS-PAH) assembly. Silk was then spin-cast from 2 mg/mL aqueous solution on a surface of PAH-terminated (PAH-PSS)₂-PAH film, or by conventional adsorption by dipping the wafers into silk solutions. Unbound silk was then removed by extensive rinsing with water. The films were released from silicon substrates by exposure to acetone to be used for TEM studies. The formation of gold nanoparticles was achieved by immersing the silk films into 1 mM HAuCl₄ solution at room temperature in 0.1 M borate buffer at pH 10.5 or into water at pH 3 for 10 h followed by extensive rinsing with Nanopure water.

ATR-FTIR Measurements. LbL assembly, silk deposition, and mineralization were monitored by infrared spectroscopy using ATR-FTIR. A Bruker FTIR spectrometer (Vertex 70) was

equipped with a narrow-band mercury cadmium telluride detector. The internal compartment of the FTIR spectrometer containing the liquid cell was purged with dry nitrogen. The ATR surface was rectangular trapezoidal multiple reflection Si or Ge crystals of dimension 50 mm \times 10 mm \times 2 mm (Harrick Scientific) whose beam entrance and exit surfaces were cut at 45 degrees. Interferograms were collected at 4 cm^{-1} resolution, and the number of averaged scans was 120. Each interferogram was corrected on the corresponding background, measured for the same ATR cell with the same D₂O buffer solution. The bare ATR crystal was used as a background. To eliminate overlap of the IR bands in the 1700–1500 cm^{-1} region with the strong water band, D₂O with 99.9% isotope content was utilized.

Multilayer films of (PSS-PAH)_n were deposited on a hydrophilic Si or Ge crystal in situ within the flow-through ATR-FTIR liquid cell. Use of multiple-reflection ATR along with a custom-made flow-trough liquid cell allowed us in situ deposition and compositional monitoring of ultrathin films (~several nanometers in thickness). Briefly, 0.1 mg/mL aqueous solutions of PAH were adsorbed onto the surface of the oxidized Si or Ge crystals at a pH 5 for 10 min, and after that the polymer solution was replaced by D₂O without polymer. A PSS was then deposited from 0.1 mg/mL solution and the deposition cycle was repeated. Silk was adsorbed in a similar way to PSS-coated surface from 0.5 mg/mL solution at pH 7. Gold mineralization was also performed in situ by filling the cell with 1 mM HAuCl₄ solution at pH 10.5 in D₂O solution, keeping the crystal exposed to the solution for 10 h followed by extensive rinsing with the buffer D₂O solution.

To study the effect of drying on silk structure, the liquid cell, with the crystal retained inside the cell, was purged with dry air or nitrogen. The spectra of silk were obtained by referring the silk spectrum to a background of a dry clean crystal. For drop-cast experiments, 2 mg/mL D₂O solution of silk was dropped on one side of ATR Si or Ge crystals. The spectrum of the dry cast film was obtained in a flow-trough cell by taking the dry clean crystal as a background.

The absorption peaks were baseline-corrected and analyzed with Galactic Grams/32 software using curve-fitting of the absorption peaks as described elsewhere.⁵¹ In the fitting procedure the wavenumbers, widths, and Gaussian band profiles were fixed, but peak intensities were varied for different spectra. The deconvolution of protein amide I region (1600–1700 cm^{-1}) into peaks corresponding to the turns, α -helix, β -sheet, and unordered structures is well reported in the literature as described in the Results and Discussion section below. However, by applying spectra deconvolution, we not only separated the absorbances typical for random coil and β -sheet structures but also confirm the positions of the protein peaks. The relative contributions of components were obtained by integration of the band areas.

Results and Discussion

A schematic presentation of the biotemplated synthesis of gold nanoparticles at interfaces is shown Figure 1. A redox-active silk molecular layer was prepared by either spin-assisted deposition or conventional adsorption on silicon wafers precoated with a (PSS-PAH)₂ layer (see section for the detailed deposition description). The polyelectrolyte matrix of 5 nm in thickness was used to

(46) Tsukruk, V. V. *Rubber Chem. Technol.* **1997**, *70*, 430.

(47) Tsukruk, V. V.; Reneker, D. H. *Polymer* **1995**, *36*, 1791.

(48) Jiang, C.; Markutsya, S.; Pikus, Y.; Tsukruk, V. *Adv. Mater.* **2004**, *16*, 157.

(49) Markutsya, S.; Jiang, C.; Pikus, Y.; Tsukruk, V. V. *Adv. Funct. Mater.* **2005**, *15*, 771.

(50) Jiang, C.; Tsukruk, V. V. *Adv. Mater.* **2006**, *18*, 829.

(51) Izumrudov, V.; Kharlampieva, E.; Sukhishvili, S. A. *Biomacromolecules* **2005**, *6*, 1782.

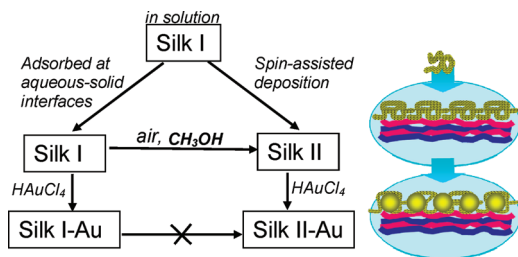


Figure 1. Transitions from silk I into silk II induced by deposition conditions, post-depositional treatments, or gold reduction.

enhance silk adhesion to the surface and provide mechanical stability upon gold synthesis. Since mineralization of the silk-tethered surface is performed at pH 10, where silk is negatively charged ($pI \sim 5$),⁵² an underlying positively charged PAH layer provides strong electrostatic interaction with silk and favors silk adhesion during mineralization.

Reducing Capability of Spin-Cast Silk. Our first focus was on examining the reduction capacity of silk-tethered films prepared by spin-assisted deposition. AFM analysis shows that silk has light-grainy morphology with a surface roughness of 3.0 ± 0.2 nm within $1 \times 1 \mu\text{m}^2$ (Figure 2a). The thickness of the silk layer was 5 nm as measured with ellipsometry. The values on thickness and roughness of the individual silk layer correlate well with those previously found for silk films.¹⁷ To perform mineralization, the film was exposed to HAuCl_4 at pH 10. The exposure results in a slight increase in surface roughness to 3.5 ± 0.2 nm.

To confirm the presence of gold nanoparticles, the organic matrix, which involved silk and polyelectrolyte layers, was burned out at 500°C as described in our recent study on poly-L-tyrosine (pTyr) containing films.⁵³ As a result, gold nanoparticles with a diameter of 7.0 ± 1.5 nm appeared evenly distributed over the substrate with no large microscale aggregates present on the surface (Figure 2b,c,d). Note that in our previous work on pTyr-tethered films we studied the effect of underlying polyelectrolyte PAH-PSS matrix on gold reduction and found that the matrix does not affect mineralization and the reduction was fostered by the top pTyr layer.⁵³ In particular, no morphological changes were observed with PSS-terminated film after its immersion into HAuCl_4 /borate reducing solution for 5 days. In contrast, PAH-terminated films demonstrated severe nanoparticle coagulation which form clusters of tens of micrometers in size. The results indicate that the covering of PAH-tethered films with an additional layer suppresses PAH reducing activity.⁵³

To further study whether silk is able reduce gold at ambient conditions, UV analysis was performed on silk-tethered films prepared on quartz slide and exposed to a reducing solution. The mineralized film showed a

characteristic band of silk at 228 nm^{54} and a distinctive UV absorption band centered at 547 nm , which corresponds to gold nanoparticles with a diameter below 50 nm^{55} (Figure 3a). Independently, TEM analysis of free-standing silk-tethered films demonstrates the gold reducing capacity. TEM images revealed individual gold nanoparticles uniformly distributed over the surface with diameters of $6.7 \pm 1.4 \text{ nm}$ (Figure 4a–c). The dimensions of nanoparticles found from TEM were close to those measured from AFM images ($7.0 \pm 1.5 \text{ nm}$). The EDAX spectrum of these films illustrates two characteristic bands of Au which confirms their composition (Figure 4d). We also found that gold nanoparticles were successfully formed on the free-standing films coated with silk. No difference in particle sizes or distributions on the free-suspended films when compared to those grown on solid templates was observed (data not shown).

The ability of silk to reduce gold nanoparticles was shown previously in bulk silk-fibroin solutions mixed with an aqueous HAuCl_4 at alkaline conditions.⁴¹ It has been reported that silk fostered the reduction of metal nanoparticles which involves tyrosine groups ionized at basic pH.⁴¹ In fact, tyrosine-containing molecules have been shown to be excellent reducing agents for synthesis and stabilization of metal nanoparticles in alkaline water^{56,57} or water/alcohol^{58,59} solutions as a result of electron transfer mechanism from tyrosine phenolic groups, which are ionized at high pH, to the respective metal ion.⁶⁰ We have recently shown that pTyr acts as an organic template and is able to direct gold nanoparticle formation to solid surfaces at ambient conditions. The reducing activity of tyrosine groups in pTyr was activated by immersing pTyr decorated surface into borate buffer at pH 10.⁵³ Our results on silk-induced mineralization indicate that tyrosine groups in silk are capable of gold reduction at mild alkaline conditions (borate buffer) similar to those in pTyr.⁵³

On the other hand, silk fibers were also found to reduce metal nanoparticles regardless of pH values. Thus, silver or gold particles were formed on silk fibers at neutral pH when tyrosine residues were nonionized.^{23,24} This phenomenon of metal reduction in a wide range of pHs was explained by the “frozen” ionized functionality as a result of treatment with sodium carbonate during preparation of silk fibers.²³

To study the effect of pH on reduction activity of a silk molecular layer, we exploited aqueous HAuCl_4 solution

(52) Hawley, T. G. Jr.; Johnson, T. B. *Ind. Eng. Chem.* **1930**, *22*, 297.

(53) Kharlampieva, E.; Slocik, J. M.; Tsukruk, T.; Naik, R. R.; Tsukruk, V. V. *Chem. Mater.* **2008**, *20*, 5822.

(54) Wang, X.; Kim, H. J.; Matsumoto, P. X.; Kaplan, D. *Langmuir* **2005**, *21*, 11335.

(55) Wang, B.; Chen, K.; Jiang, S.; Reincke, F.; Tong, W.; Wang, D.; Gao, C. Y. *Biomacromolecules* **2006**, *7*, 1203.

(56) Selvakannan, P. R.; Swami, A.; Srisathyanarayanan, D.; Shirude, P. S.; Pasricha, R.; Mandale, A. B.; Sastry, M. *Langmuir* **2004**, *20*, 7825.

(57) Bhargava, S. K.; Booth, J. M.; Agrawal, S.; Coloe, P.; Kar, G. *Langmuir* **2005**, *21*, 5949.

(58) Si, S.; Bhattacharjee, R. R.; Banerjee, A.; Mandal, T. K. *Chem.—Eur. J.* **2006**, *12*, 1256.

(59) Bhattacharjee, R. R.; Das, A. K.; Haldar, D.; Si, S.; Banerjee, A.; Mandal, T. K. *J. Nanosci. Nanotechnol.* **2005**, *5*, 1141.

(60) Ray, S.; Das, A. K.; Banerjee, A. *Chem. Commun.* **2006**, 2816.

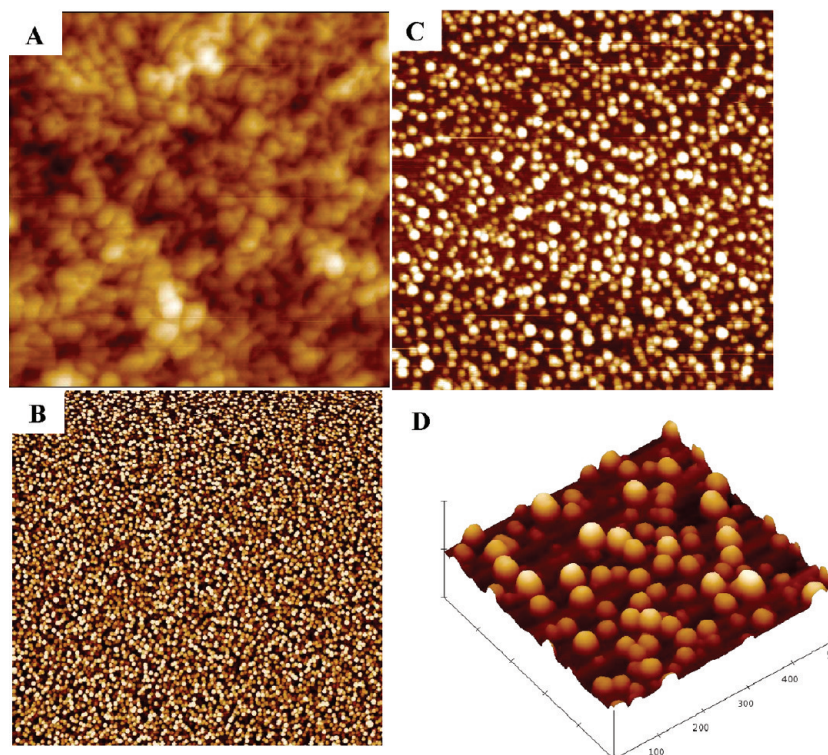


Figure 2. AFM images of a $(\text{PAH-PSS})_2\text{PAH-silk}$ film before (A) and after immersing into HAuCl_4 followed by treatment at $500\text{ }^\circ\text{C}$ (C, B, D). Silk layer was obtained by spin-assisted deposition. Z-scales are 40 nm (A, D) and 10 nm (B, C). Scan sizes are 1×1 (A, C), 5×5 (B), and $500 \times 500\ \mu\text{m}^2$ (D).

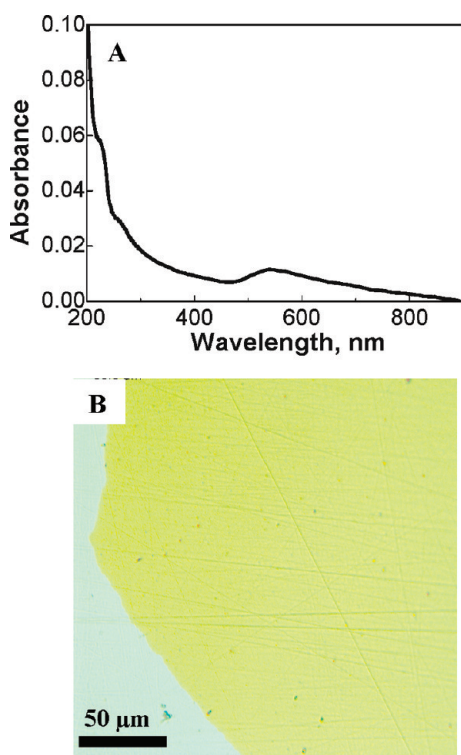


Figure 3. (A) UV spectrum of a $(\text{PAH-PSS})_2\text{PAH-silk}$ film after gold mineralization at pH 10 obtained on a quartz slide. (B) An optical image of a $(\text{PAH-PSS})_2\text{PAH-silk}$ film after gold mineralization obtained at pH 10 on a surface of an ATR Ge crystal by in situ ATR-FTIR from D_2O solutions.

at acidic pH 3. Figure 5a illustrates that individual gold nanoparticles grown under these conditions are uniformly distributed over the surface. The result indicates that alkaline conditions are not required for

silk-mediated synthesis of gold nanoparticles which is consistent with the mineralization on silk fibers.^{23,24} On the other hand, the coverage surface density is lower, but the average particle size is slightly higher (7.8 ± 1.5) than those for particles reduced at pH 10. We suggest that in our case the fewer particles at acidic conditions might be explained by fewer binding sites which can accumulate gold ions for further reduction. Indeed, at pH 10 all tyrosine groups are ionized and available for reduction as compared to a much smaller amount at pH 3 which are probably retained after silk processing.²³ The presence of ionized tyrosine groups at acidic conditions remains unclear, and further studies are needed to address this question. We also explored mineralization of silver nanoparticles on silk-tethered templates at neutral pH. We found that silk is active toward Ag synthesis, but Ag particles are very polydisperse in sizes with an average diameter of 30 ± 15 nm and form large microscopic aggregates (Figure 1S in Supporting Information).

Silk Structure at Interfaces Monitored by in Situ ATR-FTIR. Our next study was focused on investigating secondary structure of a silk layer by applying in situ ATR-FTIR, which is shown to be a surface-sensitive technique which allows resolution of protein secondary structures in ultrathin films.^{51,61,62} Figure 6a shows a representative spectrum of a 5-nm silk surface layer deposited from D_2O solution at pH 7. The spectrum illustrates a characteristic amide I band ($1600\text{--}1700\ \text{cm}^{-1}$)

(61) Gergely, C.; Bahi, S.; Szalontai, B.; Flores, H.; Schaaf, P.; Voegel, J. C.; Cuisiner, F. J. C. *Langmuir* **2004**, *20*, 5575.

(62) Malmsten, M. *Biopolymers at Interfaces*; CRC Press: New York, 2003.

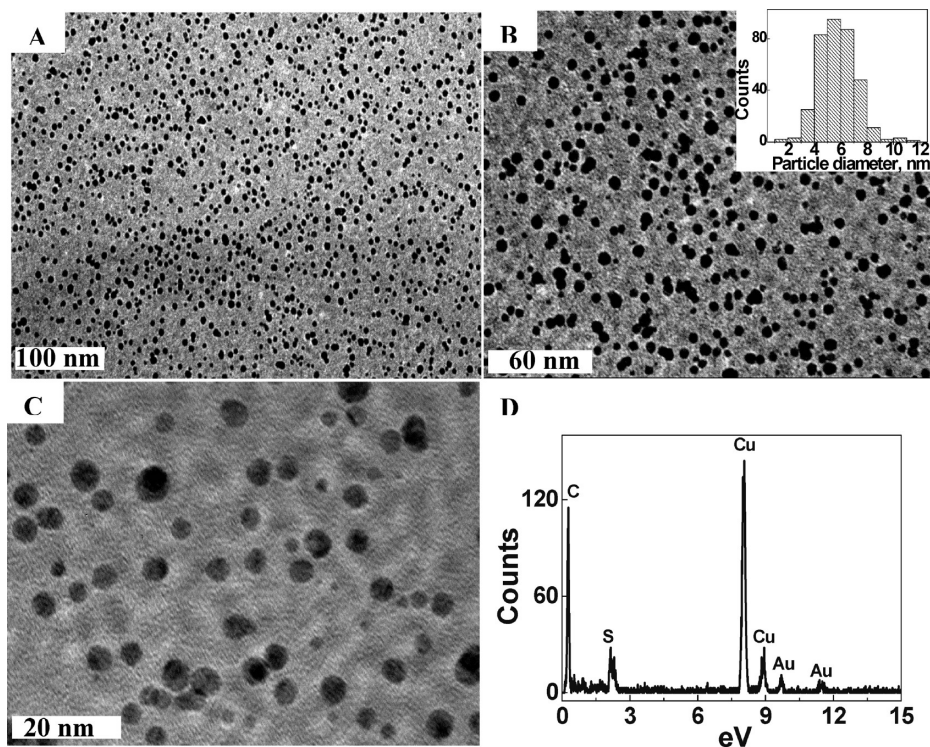


Figure 4. TEM images of free-standing (PAH-PSS)₂₀PAH-silk films after gold mineralization at pH 10 (A–C) and a corresponding EDAX spectrum (D). Silk layer was obtained via spin-assisted deposition. The histograms of nanoparticle diameters are calculated from TEM data (inset in B).

which is associated with C=O stretching in the protein backbone coupled to the N–H bending and C=N stretching modes.⁵¹ The major peak centered at 1644 cm⁻¹ correlates with silk I spectra found in D₂O solution and thus indicates that the structure of the silk molecular layer is predominantly random-coil.⁶³ To further quantitatively analyze the secondary structure of the adsorbed silk layer, contributing peaks in the amide I region were separated by using a curve-fitting procedure. (See details in the Experimental section.) In particular, the band was deconvoluted into two major Gaussian peaks centered at 1645 and 1661 cm⁻¹ associated with random coil and β -turns, respectively, while a small peak at 1683 cm⁻¹ is attributed to β -turns (Figure 6a).^{63,64} Note that random coil and α -helices, which compose silk I, cannot be distinguished by IR.⁵⁴ We have also found that the molecular layer of silk remains in the random coil conformation in wet state regardless of pH (data not shown). The result indicates that silk preserves its silk I structure (random coil conformation) when it forms a surface attached layer from solution. The same result was obtained when silk was adsorbed onto a polyelectrolyte-free Si crystal at pH 5. Thus, the underlying polyelectrolyte matrix did not affect silk structure. The result correlates well with the previous studies which showed that polyelectrolyte multilayers can create a favorable environment for the

incorporated biomolecules with no significant changes in their secondary structures and can preserve their bioactivity.^{51,65–68}

In striking contrast, an exposure of the silk layer to air results in immediate transformation of silk I into silk II (Figure 6b). Two peaks emerging at 1688 and 1623 cm⁻¹ can be attributed to crystalline β -sheets.^{64,63} The kinetics of dehydration is fast, with silk II features appearing in the spectrum in 40 s. During the next 10 min, exposure to air resulted in a gradual decrease in random-coil content (decreasing band intensity at 1645 cm⁻¹) and growth of crystalline β -sheet bands (Figure 6b). Further drying of the molecular layer of silk with nitrogen or additional exposure to methanol did not result in spectral changes. Moreover, spin-assisted deposition immediately induced silk II formation from silk I (Figure 7a). The spectrum shown in Figure 7a reveals the same features as those in Figure 6b. The deconvolution of the spectra uncovered four major bands: two of them centered at 1688 and 1623 cm⁻¹ and associated with β -sheets and two bands at 1645 and 1661 cm⁻¹ attributed to random coils. The integration of β -sheets band intensities with respect to the total integrated spectrum intensity showed 30% silk II content in the spectrum (Figure 7a). It is worth noting that similar transitions from silk I into silk II as a result of dehydration

(63) Dicko, C.; Knight, D.; Kenney, J.; Vollrath, F. *Biomacromolecules* **2004**, *5*, 2105.

(64) Hermanson, K.; Huemmerich, D.; Scheibel, T.; Bausch, A. R. *Adv. Mater.* **2007**, *19*, 1810.

(65) Ariga, K.; Kunitake, T. In *Protein Architecture, Interfacing Molecular Assemblies and Immobilization Biotechnology*; Lvov, Y., Möhwald, H., Eds.; Marcel Dekker: New York, 2000; p 169.

(66) Müller, M.; Rieser, T.; Dubin, P. L.; Lunkwitz, K. *Macromol. Rapid Commun.* **2001**, *22*, 390.

(67) Szyk, L.; Schwinte, P.; Voegel, J. C.; Schaaf, P.; Tinland, B. *J. Phys. Chem. B* **2002**, *106*, 6055.

(68) Caruso, F.; Furlong, D. N.; Ariga, K.; Ichinose, I.; Kunitake, T. *Langmuir* **1998**, *14*, 4559.

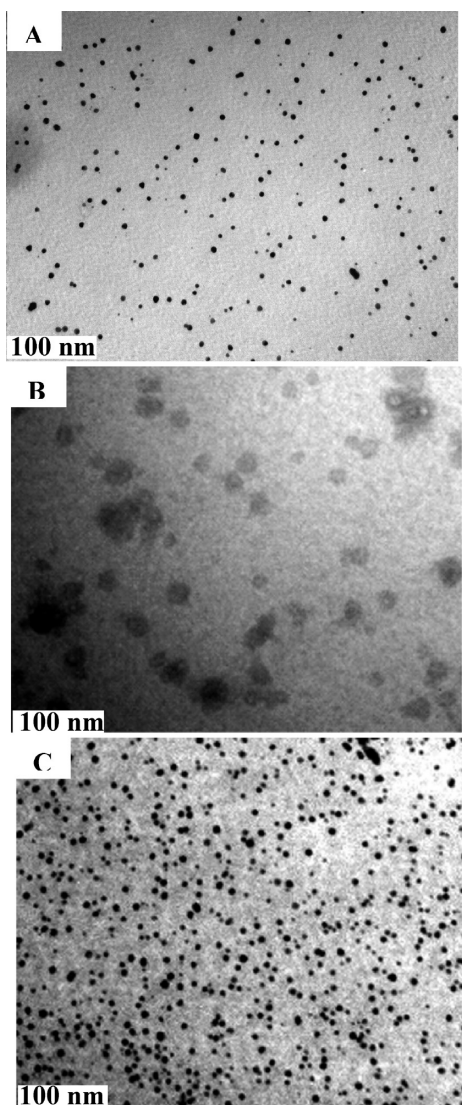


Figure 5. (A) A TEM image of a free-standing $(\text{PAH-PSS})_{20}\text{PAH}$ -silk film after gold mineralization at pH 3. Silk layer was obtained via spin-assisted deposition. (B, C) TEM images of free-standing $(\text{PAH-PSS})_{20}\text{PAH}$ -silk film after gold mineralization at pH 10. Silk layer was deposited by conventional adsorption. The film was either directly immersed into HAuCl_4 without during (B) or it was methanol treated and then immersed into HAuCl_4 (C).

can be induced for thicker films and electrospun fibers but only if treated with organic solvents or elevated temperatures.^{14,17,42,54,69–72}

In contrast, a dry spin-cast film with thickness of 100 nm shows a predominant random-coil structure under ambient conditions (Figure 7b). This result indicates that the structure of the dry ultrathin films (~ 5 nm) is different from that for the relatively thick films (~ 100 nm). Note that for the micrometer-sized silk films, the longer time (several weeks) or the stronger dehydrator like methanol are required to introduce the conforma-

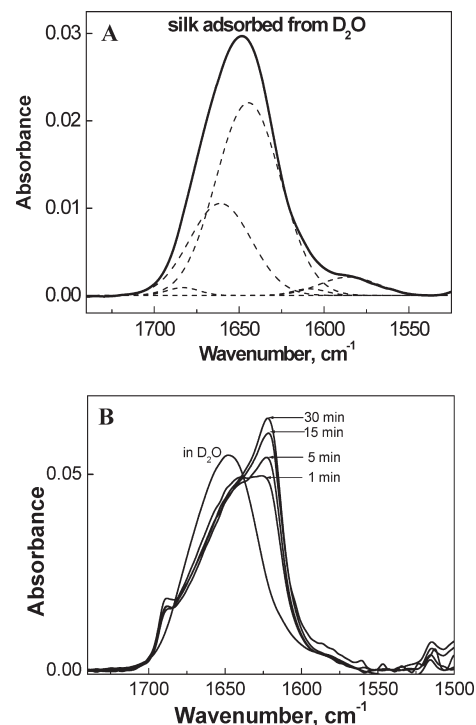


Figure 6. In-situ ATR-FTIR spectra of a silk molecular layer obtained in D_2O (A) and further exposed to air for 1–30 min (B). Silk was deposited in situ in a liquid cell from D_2O solutions on a Ge ATR crystal precoated with a $(\text{PAH-PSS})_2\text{PAH}$ film.

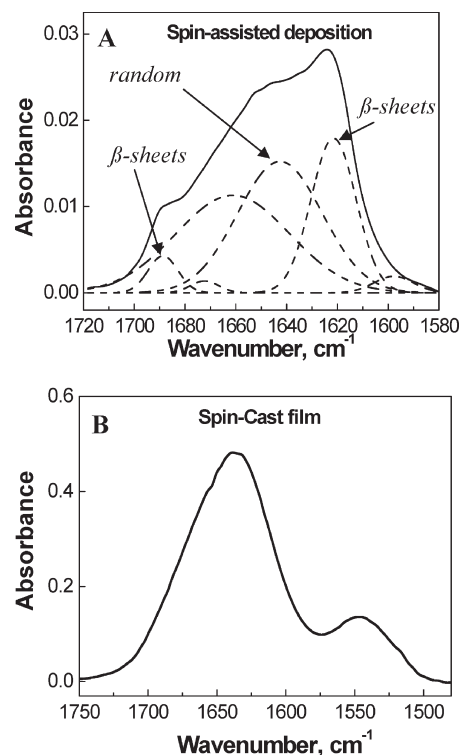


Figure 7. ATR-FTIR spectra of silk layers deposited from D_2O solutions by spin-assisted assembly (A) or by spin-casting (B) on a Ge ATR crystal precoated with a $(\text{PAH-PSS})_2\text{PAH}$ film. The $(\text{PAH-PSS})_2\text{PAH}$ films were assembled in situ in a liquid cell, dried, and taken as a background.

- (69) Drummy, L. F.; Phillips, D. M.; Stone, M. O.; Farmer, B. L.; Naik, R. R. *Biomolecules* **2005**, *6*, 3328.
 (70) Rousseau, M.-E.; Beaulieu, L.; Lefèvre, T.; Paradis, J.; Asakura, T.; Pérolet, M *Biomacromolecules* **2006**, *7*, 2512.
 (71) Hu, B.-W.; Zhou, P.; Noda, I.; Ruan, Q.-X. *J. Phys. Chem. B* **2006**, *110*, 18046.
 (72) Zong, X.-H.; Zhou, P.; Shao, Z.-Z.; Chen, S.-M.; Chen, X.; Hu, B.-W.; Deng, F.; Yao, W.-H. *Biochemistry* **2004**, *43*, 11932.

tional transition from silk I to silk II.⁴³ On the other hand, freeze-drying silk I solutions did not result in silk II transformations and the random coil conformation in a

dilute solution is maintained in the film.⁷³ Thus, we can conclude that solid templates also contribute to the fast silk I–silk II transformation in addition to the drying effect.

Similar results on conformational transition were found for poly-L-lysine, which underwent conformational changes from unstable random-coil in solutions into more stable β -sheet-rich structure in cast films.⁷⁴ It is believed that dehydration results in deswelling and close proximity of neighboring molecular fragments which promote the formation of hydrogen bonding network and hence β -sheet formation.

Effect of Silk Structure on Mineralization. To study the effect of silk secondary structure on its reduction activity, gold reduction was also performed directly on silk I (wet) layer. For that purpose, silk was allowed to adsorb on silicon wafer precoated with 20-bilayer PSS-PAH film and immediately exposed to HAuCl_4 /borate solution without drying. Figure 5b shows grown gold nanoparticles with an average diameter of 17 ± 5 nm that tend to form large coagulates up to 100 nm across. However, when silk I layer was treated with methanol to provide its transformation into silk II, the reduced nanoparticles were found to be 6.9 ± 1.1 nm in diameter (Figure 5c), close to that obtained on spin-assisted silk layers (Figure 4a).

The results indicate that the presence of β -sheets is not critical for nanoparticle growth, but it is important for the particle sizes and monodispersity. We have earlier found that the biotemplated surface-mediated approach provides formation of individual and monodisperse titania or gold nanoparticles.^{53,75,76} For example, homogeneously distributed rSilC domains on polyelectrolyte surface represented “nanoreactors” for confined titania synthesis. These surface domains consisted of random coil and β -sheet mixture and prevented the aggregation of nanoparticles. In contrast, rSilC being in unordered random-coil conformation in solution cannot provide nanoparticle size uniformity which results in micro-sized TiO_2 aggregates.⁷⁶ We suggest that similar to rSilC the presence of β -sheets in silk II can provide tyrosine ordering in the surface domains seen as silk grainy morphology in Figure 2a. The silk domains facilitate formation of individual, gold nanoparticles, prevent their aggregation, and limit their dimensions to 6 nm, in contrast to large aggregates in silk I.

In situ ATR-FTIR was then applied to study the effect of nanoparticle reduction on silk I or silk II conformations. Figure 8a,b shows no difference in the spectra of both silk I and II before and after mineralization

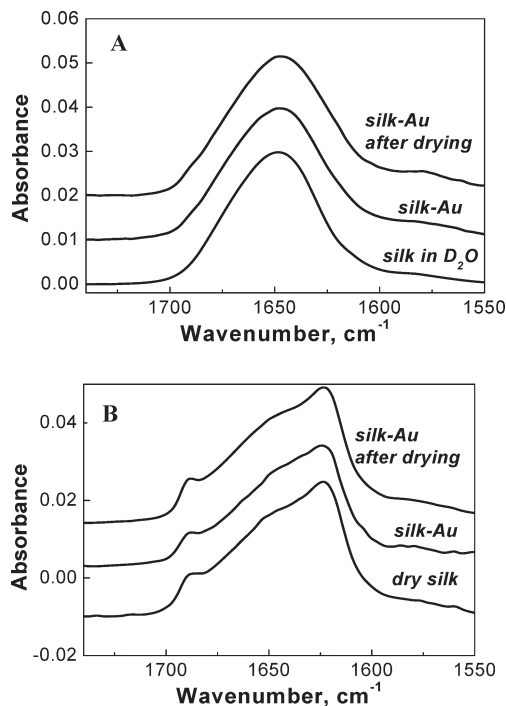


Figure 8. (A) ATR-FTIR spectra of silk I layer obtained before mineralization, after mineralization, and dried after mineralization. (B) ATR-FTIR spectra of a silk II layer produced by spin-assisted deposition and obtained before mineralization, after mineralization, and dried after mineralization. The films were prepared from D_2O solutions on a Ge ATR crystal precoated with a $(\text{PAH-PSS})_2\text{PAH}$ film. Silk I was deposited in situ in a liquid cell and further dried to be transformed into silk II. Mineralization in both cases was performed in the liquid cell.

indicating that gold formation does not induce any conformational changes in silk structures. It was previously reported that partial structural transition from silk I to silk II occurred as a result of titania mineralization in silk fibroin solutions.²⁰ However, when silk forms a 5-nm film, we found no transformational changes in the spectrum of a dry silk I–Au film and in that for the wet film before mineralization (Figure 8a). Moreover, silk I being mineralized preserved its secondary structure not just upon reduction but also upon further drying. The spectrum of dry gold nanoparticle containing silk I layer clearly shows predominant random-coil structure similar to that before mineralization, indicating no transition into silk II upon drying (Figure 8a). An optical image of the film after drying is illustrated in Figure 3b. We suggest that in our case the random structure is preserved due to constrained chain mobility and the capability to reorganization induced by the presence of grown gold particles and very limited overall thickness of silk layer (5 nm). Moreover, hydrogen-bonding can be suppressed due to the “deactivation” of tyrosine groups under mild reduction conditions.¹⁸

In summary, we demonstrated an application of silk as a 5-nm redox-active template for controllable, one-step synthesis of gold nanoparticles via control over silk secondary structure and revealed a “diagram” of states presented in Figure 1. Specifically, we used in situ-ATR-FTIR to follow interfacial conformational changes of silk ultrathin films and found that the film preserves

(73) Magoshi, J.; Magoshi, Y.; Becker, M. A.; Kato, M.; Han, Z.; Tanaka, T.; Inoue, S.-I.; Nakamura, S. *Thermochim. Acta* **2000**, *352*, 165.

(74) Safar, J.; Roller, P. P.; Ruben, G. C.; Gajdusek, D. C.; Gibbs, C. J. *Biopolymers* **1993**, *33*, 1461.

(75) Kharlampieva, E.; Tsukruk, T.; Slocik, J. M.; Ko, H.; Poulsen, N.; Naik, R. R.; Kroger, N.; Tsukruk, V. V. *Adv. Mater.* **2008**, *20*, 3274.

(76) Kharlampieva, E.; Slocik, J. M.; Singamaneni, S.; Poulsen, N.; Kroger, N.; Naik, R. R.; Tsukruk, V. V. *Adv. Funct. Mater.* **2009**, doi: 10.1002/adfm.200801825.

native-like silk I structure in wet form, but can be rapidly transformed into silk II upon simple exposure to air and, therefore, remains stable against dissolution without treatment with organic solvents during mineralization. We found that both silk I and silk II molecular layers can facilitate gold nanoparticle formation at ambient conditions, suggesting that tyrosine groups are available for metal ion reduction in both forms of silk. We suggest that the presence of β -sheets in silk II facilitate tyrosine ordering, which results in the formation of individual, monodisperse nanoparticles, prevents their aggregation, and limits their dimensions to 6 nm. In addition, the reduction does not transform initial secondary structure of both silk I and II forms and silk I after being mineralized preserved its structure from further transformation

into silk II even upon drying. These results are critical for the better understanding of silk interfacial behavior and offer an opportunity to design a new class of nanocomposites that combine the beneficial features of silk with those of the nanoparticles.

Acknowledgment. This work was supported by the Air Force Office for Scientific Research FA9550-08-1-0446 project, Air Force Research Laboratory, and AFRL Bio-X STT program.

Supporting Information Available: TEM images of free-standing (PAH-PSS)₂₀PAH-silk-Ag films with the corresponding EDX spectrum (Figure 1S) (PDF). This material is available free of charge via the Internet at <http://pubs.acs.org>.